

# Physical parameters of two very cool T dwarfs

D. Saumon

*Los Alamos National Laboratory, MS P365, Los Alamos, NM 87545*

[dsaumon@lanl.gov](mailto:dsaumon@lanl.gov)

M. S. Marley

*MS 245-3, NASA Ames Research Center, Moffett Field, CA 94035*

S. K. Leggett and T. R. Geballe

*Gemini Observatory, 670 N. A'ohoku Place, Hilo, HI 96720*

D. Stephens and D. A. Golimowski

*Department of Physics & Astronomy, Johns Hopkins University, 3400 North Charles Street, Baltimore, MD 21218*

M. C. Cushing<sup>1</sup> and X. Fan

*Steward Observatory, 933 N. Cherry Avenue, Tucson, AZ 85721*

J. T. Rayner

*Institute for Astronomy, University of Hawaii, 2680 Woodlawn Drive, Honolulu, HI 96822*

K. Lodders

*Dept. of Earth & Planetary Science, Washington University, St. Louis, MO 63130*

and

R. S. Freedman

*SETI Institute, MS 245-3, NASA Ames Research Center, Moffett Field, CA 94035*

## ABSTRACT

---

<sup>1</sup>*Spitzer Fellow*

We present new infrared spectra of the T8 brown dwarf 2MASS J04151954–0935066: 2.9–4.1  $\mu\text{m}$  spectra obtained with the Infrared Camera and Spectrograph on the Subaru Telescope, and 5.2–14.5  $\mu\text{m}$  spectra obtained with the Infrared Spectrograph on the *Spitzer Space Telescope*. We use these data and models to determine an accurate bolometric luminosity of  $\log L_{\text{bol}}/L_{\odot} = -5.67$  and to constrain the effective temperature, gravity, mass and age to 725–775 K,  $\log g = 5.00\text{--}5.37$ ,  $M = 33\text{--}58 M_{\text{Jupiter}}$  and age=3–10Gyr. We perform the same analysis using published 0.6–15  $\mu\text{m}$  spectra for the T7.5 dwarf 2MASS J12171110–0311131, for which we find a metal-rich composition ( $[\text{Fe}/\text{H}] \sim 0.3$ ), and  $\log L_{\text{bol}}/L_{\odot} = -5.31$ ,  $T_{\text{eff}} = 850\text{--}950$  K,  $\log g = 4.80\text{--}5.42$ ,  $M = 25\text{--}66 M_{\text{Jupiter}}$  and age=1–10Gyr. These luminosities and effective temperatures straddle those determined with the same method and models for Gl 570D by Saumon et al. (2006) and make 2MASS J04151954–0935066 the coolest and least luminous T dwarf with well-determined properties. We find that synthetic spectra generated by the models reproduce the observed red through mid-infrared spectra of 2MASS J04151954–0935066 and 2MASS J12171110–0311131 very well, except for known discrepancies which are most likely due to the incomplete  $\text{CH}_4$  opacities. Both objects show evidence of departures from strict chemical equilibrium and we discuss this result in the context of other late T dwarfs where disequilibrium phenomena have been observed.

*Subject headings:* stars: low-mass, brown dwarfs — stars: individual (2MASS J04151954–0935066, 2MASS J12171110–0311131, Gl 570D)

## 1. Introduction

The Sloan Digital Sky Survey (SDSS; York et al. 2000) and the Two Micron All Sky Survey (2MASS; Beichman et al. (1998); Skrutskie et al. (2006)) have revealed large numbers of ultracool low-mass field dwarfs, known as L and T dwarfs. The effective temperatures ( $T_{\text{eff}}$ ) of L dwarfs are  $\sim 1450\text{--}2200$  K, and those of currently known T dwarfs are  $\sim 700\text{--}1450$  K (Golimowski et al. 2004; Vrba et al. 2004). T dwarfs are identified by the presence of  $\text{CH}_4$  absorption features in both the  $H$  and  $K$  near-infrared bands, the  $2\nu_2 + \nu_3$  and  $2\nu_3$  features at 1.63 and 1.67  $\mu\text{m}$ , the P-branch of the  $\nu_2 + \nu_3$  band at 2.20  $\mu\text{m}$ , and the  $\nu_3 + \nu_4$  and  $\nu_1 + \nu_4$  bands at 2.32 and 2.37  $\mu\text{m}$ . Spectral classification schemes using near-infrared spectra have been presented for T dwarfs by Burgasser et al. (2002); Geballe et al. (2002). These similar schemes, using primarily the strengths of the  $\text{H}_2\text{O}$  and  $\text{CH}_4$  absorption features at 1–2.5  $\mu\text{m}$ , were recently merged by Burgasser et al. (2006a).

Currently, there are six dwarfs known that are classified as later than T7. Five of these were discovered in the 2MASS database: 2MASS J04151954–0935066, 2MASS J09393548–2448279, 2MASS J11145133–2618235, 2MASS J12171110-0311131 and 2MASS J14571496–2121477 (Burgasser et al. 1999, 2000, 2002, Tinney et al. 2005). The sixth, HD3651B, was recently discovered through searches for wide companions to stars known to host extrasolar planets (Mugrauer et al. 2006; Luhman et al. 2006). Trigonometric parallaxes have been published for four of these dwarfs and Table 1 lists these four objects. Full 2MASS names are given in the Table, but in the rest of this paper we use abbreviated names in the form 2MASS JHHMM±DDMM, except for 2MASS J14571496–2121477 which we refer to by its more commonly used name of Gl 570D. Table 1 lists published values of trigonometric parallax, tangential velocity, bolometric luminosity, effective temperature ( $T_{\text{eff}}$ ), and surface gravity ( $g$ ).

Three of the very late T dwarfs, 2MASS J0415–0935, 2MASS J1217–0311 and Gl 570D, have been observed spectroscopically in the mid-infrared, and they form the sample for this paper. Only near-infrared spectra are available for the other three known T7.5–T8 dwarfs and these will be discussed in a future publication. Figure 1 plots the red and near-infrared spectra for the three dwarfs in our sample. It can be seen that the bands of H<sub>2</sub>O and CH<sub>4</sub> are extremely strong, as is the K I 0.77  $\mu\text{m}$  doublet. Narrow peaks of flux emerge from between these bands.

In this paper we present new 2.9–4.1  $\mu\text{m}$  and 5.5–15  $\mu\text{m}$  low-resolution spectra of one of our sample, 2MASS J0415–0935 (T8). The former were obtained using the Infrared Camera and Spectrograph (IRCS; Kobayashi et al. 2000) on the Subaru Telescope on Mauna Kea, and the latter using the Infrared Spectrograph (IRS; Houck et al. 2004) on the *Spitzer Space Telescope* (Werner et al. 2004). We use these data, together with previously published red and near-infrared spectra and trigonometric parallaxes, and grids of evolutionary and atmospheric models, to determine accurate values of  $L_{\text{bol}}$ ,  $T_{\text{eff}}$  and  $\log g$  for this dwarf. We carry out the same analysis for a second member of the sample, 2MASS J1217–0311 (T7.5), using published IRS data, and compare these parameters to those derived in the same way for the third member, Gl 570D (T7.5) by Saumon et al. (2006, hereafter S06). Matches between the data and synthetic spectra generated from the atmospheric models are examined.

## 2. Observations

### 2.1. Published Observational Data

Near-infrared spectroscopy and 2MASS photometry for 2MASS J0415–0935, 2MASS J1217–0311 and Gl 570D can be found in the discovery papers (Table 1; Burgasser et al. 1999, 2000, 2002). Red spectra are presented by Burgasser et al. (2003). Near-infrared spectra are also presented by Geballe et al. (2001, 2002) for Gl 570D and 2MASS J1217–0311, and by Knapp et al. (2004) for 2MASS J0415–0935. Near-infrared spectral indices and the implied spectral types can be found for them in Burgasser et al. (2006a). Near-infrared photometry on the MKO system (Tokunaga et al. 2002) is available for Gl 570D (Geballe et al. 2001), 2MASS J1217–0311 (Leggett et al. 2002), and 2MASS J0415–0935 (Knapp et al. 2004).

Longer wavelength data are also available for our sample. Golimowski et al. (2004) present  $L'_{\text{MKO}}$  photometry for all three dwarfs, and  $M'_{\text{MKO}}$  photometry for 2MASS J0415–0935. Patten et al. (2006) give *Spitzer*'s Infrared Array Camera (IRAC; Fazio et al. 2004) photometry at 3.55, 4.49, 5.73, and 7.87  $\mu\text{m}$  for the three dwarfs. IRS 5.2–14.5  $\mu\text{m}$  spectra have been published for Gl 570D (S06), and 2MASS J1217–0311 (Cushing et al. 2006).

### 2.2. New 2.9–4.1 $\mu\text{m}$ IRCS Data

2MASS J0415–0935 was observed on the night of 2002 December 12 with the Infrared Camera and Spectrograph (IRCS; Kobayashi et al. 2000) mounted on the 8.2-m Subaru Telescope. We used the  $L$ -band grism with a slit width of 0''.6 which resulted in a spectrum covering 2.90 to 4.16  $\mu\text{m}$  at a resolving power of  $R \sim 210$ . A series of forty 35-second exposures were taken in pairs, with the target at two different positions along the 20'' slit. A nearby A0 V star, HD 29573, was also observed to correct for absorption due to the Earth's atmosphere and the instrument throughput, and a series of flat-field exposures and dark frames were taken at the end of the night.

The spectra were extracted using a modified version of the Spextool data reduction package (Cushing et al. 2004). Each pair of exposures was subtracted and then flat-fielded. The spectra were then extracted, and wavelength-calibrated using sky emission features. The target spectra were corrected for telluric absorption and the instrument throughput by dividing by the spectrum of HD 29573 and multiplying by a Planck function for a temperature of 9500 K, as appropriate for an A0 V star. The spectrum was rebinned to have 1 pixel per resolution element. The final signal to noise ratio of the spectrum ranges from 4 to 10 per binned resolution element. Flux calibration was obtained by scaling the spectrum to match

the  $L'_{\text{MKO}}$  magnitude.

### 2.3. New 5.2–14.5 $\mu\text{m}$ IRS Data

2MASS J0415–0935 was observed with the Infrared Spectrograph (IRS; Houck et al. 2004) on 2005 September 6, using the *Spitzer Space Telescope* as part of our General Observer Cycle 1 campaign to obtain mid-infrared spectra for a number of late-L and T dwarfs. The Short-Low (SL) module was used to obtain both second-order (5.2–7.7  $\mu\text{m}$ ) and first-order (7.4–14.5  $\mu\text{m}$ ) spectra in staring mode. Two first-order and one second-order sequences were acquired. Each sequence consisted of 18 observations taken at one position along either the first-order or second-order slit, followed by a nod to a second position on the slit for an additional 18 observations. The data were processed using version 13.2.0 of the IRS pipeline, which removed all of the “Spitzer-specific” effects and produced a Basic Calibrated Data (BCD) image for each observation.

The BCD images were reduced using various scripts and contributed IDL software. First, a mask identifying bad pixels was created by flagging those pixels that were variable with time, unstable or “Not-a-Number” (NAN) during the course of observations. The images and mask were then run through version 1.5 of the IRSCLEAN\_MASK routine (available from the Spitzer Science Center) to correct the bad pixels. The sky background in each image was removed by combining all of the data in the same order, but other nod position, using a median-rejection algorithm, and subtracting the resulting sky frame. The residual background in each subtracted image was removed by taking the median value of the background on a row-by-row basis and then subtracting the value for each row. After a final visual inspection of the images, the data were loaded into the Spectroscopic Modeling Analysis and Reduction Tool (SMART, Higdon et al. 2004) for extraction and wavelength calibration, using a fixed-width aperture of 3 pixels. All of the spectra taken in the same order and nod position were combined using a mean-clipping algorithm. IRS observations of the standard star HR 6348, taken on September 9 and 14 2005, were similarly combined and extracted, and a spectral template provided by G. C. Sloan was used to determine the relative spectral response for each order and nod position. These response functions were used to correct for the instrumental response and to produce an initial flux-calibration for the 2MASS J0415–0935 spectra. The spectra in each order were combined and the two orders merged to produce a single spectrum from 5.2 to 14.5  $\mu\text{m}$ . IRAC Channel 4 photometry from Patten et al. (2006) was used to produce a final flux calibration — the spectra were scaled by a constant to produce a match to the photometry.

The new IRS spectrum of 2MASS J0415–0935 and the published spectra for Gl 570D and

2MASS J1217–0311 are shown in Figure 2, with the principal absorbing species identified. Note that 2MASS J1217–0311 is located in a part of the sky having a high mid-infrared background, leading to a somewhat noisier spectrum than the other two T dwarfs.

### 3. Evolution of Brown Dwarfs: Age, Mass, Gravity and Luminosity

Brown dwarfs cool as they age with a cooling rate dependent on the mass. Hence both mass and age are fundamental parameters for these objects. For field brown dwarfs, such as those in Table 1, constraining the age is a challenge. In contrast, HD3651B and Gl 570D are companions to K-type main sequence stars, which allows age to be constrained based on kinematics, X-ray luminosity, H $\alpha$  and Ca II H and K emission. Liu et al. (2006) show that HD3651B is aged 3–12 Gyr and Gl 570D 1–5 Gyr. Kinematic information only is available for 2MASS J0415–0935 and 2MASS J1217–0311. These dwarfs have  $V_{\tan} \sim 50$ –60 km/s, suggesting that their ages lie in the range 1–10 Gyr, and that neither is very young, nor are they likely to be halo members (see for example the discussion of kinematics in the solar region by Eggen (1998) and references therein).

A convenient feature of brown dwarfs is that the mass-radius relation shows a broad maximum at  $\sim 4 M_{\text{Jupiter}}$ , and that their radii are within  $\pm 30\%$  of the radius of Jupiter for masses 0.3–70  $M_{\text{Jupiter}}$  and ages  $\gtrsim 200$  Myr (Figure 3 of Burrows et al. (2001)). This peak results from the balance between electron degeneracy pressure, which dominates in the more massive brown dwarfs, and electrostatic repulsion of atoms and molecules, which dominates at the lower masses. With a nearly constant radius over more than a two order of magnitude variation in mass, the gravity of a brown dwarf is closely correlated to its mass and is approximately independent of age for older brown dwarfs such as those in our sample (Figure 3).

S06 use the observed integrated flux and atmospheric and evolutionary models to derive  $\log g = 5.09 - 5.23$  for Gl 570D, corresponding to a mass of 38–47  $M_{\text{Jupiter}}$ . Burgasser et al. (2006b) use measured and modelled near-infrared spectral indices to determine  $T_{\text{eff}}$  and  $\log g$  for a sample of T dwarfs, using the well-determined values for Gl 570D as calibration of the method; their values are given in Table 1. The value for Gl 570D agrees with that determined by S06, as would be expected. Applying the spectral indices technique to HD 3651B, Burgasser (2006) derives  $\log g = 4.7 - 5.1$  and mass 20–40  $M_{\text{Jupiter}}$ , whereas luminosity arguments (Luhman et al. 2006; Liu et al. 2006) imply  $\log g = 5.1 - 5.5$  and mass 40–70  $M_{\text{Jupiter}}$ . The values of  $\log g$  derived by Burgasser et al. (2006b) for 2MASS J1217–0311 and 2MASS J0415–0935 are consistent with the estimates made by Knapp et al. (2004) based on  $H - K$  color (also shown in Table 1), and suggest masses of 20–30 and 25–35

$M_{\text{Jupiter}}$ , respectively.

Here we analyze the brown dwarfs 2MASS J1217–0311 and 2MASS J0415–0935 with the same method as described in S06 for Gl 570D, which is based on the integrated observed flux. The model atmospheres, spectra and evolutionary sequences that are the basis for our analysis of the spectroscopic and photometric data are described briefly in §4. Section 5 presents the values of  $T_{\text{eff}}$ ,  $\log g$ , luminosity, mass, radius, and age we have obtained for 2MASS J1217–0311 and 2MASS J0415–0935, along with the values for Gl 570D from S06. In §6, we perform fits of the spectroscopic and photometric data to further constrain the range of acceptable parameters, including metallicity, and explore the possibility of non-equilibrium chemistry in their atmospheres.

#### 4. Models: Evolution and Spectra

To constrain the properties of the T dwarfs in our sample with known parallax and mid-infrared spectra, we follow the procedure detailed in S06, Geballe et al. (2001), and Saumon et al. (2000). The method uses synthetic spectra to fill in gaps in the spectral coverage and complement the data at long wavelengths, in order to obtain a bolometric correction. For objects with measured parallax, this bolometric correction is computed self-consistently with evolutionary models which give the radius and the bolometric luminosity of the brown dwarf. There are no assumptions beyond those that are implicit in the computation of the atmosphere models, synthetic spectra and evolution. Because we are studying late T dwarfs, the entire analysis is based on cloudless model atmospheres.

For solar metallicity, the models used here are the same as those used for Gl 570D by S06. The chemical equilibrium calculations for the atmosphere models are described in Lodders & Fegley (2002) and use the solar abundances of Lodders (2003). In addition, we have computed a grid of atmosphere models and associated evolutionary tracks for a non-solar metallicity of  $[\text{Fe}/\text{H}] = +0.3$ . The non-solar sequences use exactly the same interior physics as the solar sequence; only the surface boundary condition, which is extracted from the model atmospheres, is different.

There is growing evidence that the abundances of  $\text{NH}_3$  and  $\text{CO}$  in the atmospheres of late T dwarfs can differ substantially from those expected from chemical equilibrium. The observed abundances for these two species can be simply explained as departures from chemical equilibrium driven by vertical mixing in the atmospheres (Fegley & Lodders 1996; Lodders & Fegley 2002; Griffith & Yelle 1999; Noll et al. 1997; Saumon et al. 2000, 2003, 2006), a phenomenon that has been recognized in giant planets for some time now

(Prinn & Barshay 1977; Fegley & Lodders 1994; Bézard et al. 2002). In the lower atmosphere, which is convective, the mixing time scale over one pressure scale height  $H_p$  is very short  $\tau_{\text{mix}} = H_p/v_{\text{conv}} \sim 1$  s), where  $v_{\text{conv}}$  is the convective velocity computed from the mixing length theory of convection. Thus, the mixing time scale in the convection zone comes from the mixing length formalism and it is not adjustable. In the overlying radiative zone, the physical cause for the mixing is presently unknown and could arise from the turbulent dissipation of waves generated at the convective/radiative boundary, meridional circulation, or differential rotation, for example. Such processes are expected to mix the radiative atmosphere on much longer time scales than convection. For modeling purposes, we treat the mixing time scale *in the radiative zone* as a free parameter, parametrized by the coefficient of eddy diffusivity,  $K_{zz}$ . We consider values in the range  $\log K_{zz}(\text{cm}^2 \text{s}^{-1}) = 2$  to 6, which corresponds to  $\tau_{\text{mix}} = H_p^2/K_{zz} \sim 10$  yr to  $\sim 1$  h, respectively, in the atmospheres of late T dwarfs. For comparison,  $K_{zz}$  would have to be of the order of  $10^7$  to  $10^9 \text{ cm}^2 \text{s}^{-1}$  to get mixing time scales as short as those found in the convection zone. Since the IRS spectra and 4–5  $\mu\text{m}$  photometry probe a band of  $\text{NH}_3$  and a band of CO, respectively, we will consider departures from chemical equilibrium caused by vertical mixing in comparing our models with the data.

## 5. Determination of the Physical Parameters of 2MASS J0415–0935 and 2MASS J1217–0311

Bolometric luminosities have previously been determined for Gl 570D, 2MASS J1217–0311 and 2MASS J0415–0935 by Geballe et al. (2001) and Golimowski et al. (2004). These authors used the measured parallaxes for these dwarfs and the observed red through 5  $\mu\text{m}$  spectral energy distributions, with an extrapolation to longer wavelengths, to obtain the emitted flux. The validity of the long-wavelength extrapolation has been verified by Cushing et al. (2006), who combine *Spitzer* mid-infrared data with shorter wavelength data to determine bolometric luminosities for a sample of M1–T5 dwarfs. Their luminosities agree with those of Golimowski et al. (2004) within the latter’s  $\sim 10\%$  uncertainties. Also, S06 repeats the Geballe et al. (2001) study of Gl 570D, adding mid-infrared spectra, and find good agreement with the earlier study.

Here we rederive  $L_{\text{bol}}$ ,  $T_{\text{eff}}$  and  $\log g$  for 2MASS J0415–0935 and 2MASS J1217–0311 using the method developed in Saumon et al. (2000) for Gl 229B, which has also been applied to Gl 570D (Geballe et al. 2001; Saumon et al. 2006). The method can be applied to brown dwarfs of known parallax and is not sensitive to systematic problems present in the synthetic spectra, as opposed to direct fitting of the observed spectra which would be

affected by such problems. For brown dwarfs with a well-sampled spectral energy distribution ( $\gtrsim 50\%$  of the flux), the method has been shown to be very robust.

We have first summed the observed fluxes using red spectra (Burgasser et al. 2003), near-infrared spectra (Geballe et al. 2002; Knapp et al. 2004),  $3\mu\text{m}$  spectra where available (this work) and IRS spectra (this work and Cushing et al. 2006). The  $1\text{--}4\mu\text{m}$  spectra are flux calibrated using accurate MKO-system  $JHKL'$  photometry from Leggett et al. (2002); Golimowski et al. (2004); Knapp et al. (2004). The IRS spectra are flux calibrated using the IRAC channel 4 photometry from Patten et al. (2006). The uncertainties in the integrated observed flux are dominated by the flux calibration uncertainties. For 2MASS J0415–0935 they are 5% at all wavelengths except for the  $1\text{--}2.5\mu\text{m}$  spectrum which has a 3% uncertainty. For 2MASS J1217–0311 they are 5% in the red, 3% in the near-infrared, and 18% at IRS wavelengths. The integrated fluxes at Earth over the observed spectral regions are  $1.532 \pm 0.057 \times 10^{-12} \text{ erg s}^{-1} \text{ cm}^{-2}$  for 2MASS J0415–0935 and  $9.67 \pm 0.55 \times 10^{-13} \text{ erg s}^{-1} \text{ cm}^{-2}$  for 2MASS J1217–0311, which in each case represents  $\sim 75\%$  of the bolometric flux. The above uncertainties are the sum of the uncertainties in each integrated segment, and thus are conservative.

Among all possible values of  $T_{\text{eff}}$  and  $\log g$ , only a small subset will give a bolometric flux correction to the above values that makes  $L_{\text{bol}}$  consistent with the evolution (mass and age) and the known parallax. In the  $\{T_{\text{eff}}, g\}$  space, this subset forms a one-dimensional curve. The location along the curve can be parametrized with the mass, age, gravity, effective temperature, luminosity or radius. So far, only age constraints and detailed spectral fitting have been used to further limit the allowed range of the solution along the one-dimensional curve. For Gl 570D, with an age of 2–5 Gyr and detailed fits of the IRS spectrum, S06 obtained  $T_{\text{eff}} = 800\text{--}820\text{ K}$ ,  $\log g = 5.09\text{--}5.23\text{ cm/s}^2$ , and mass  $38\text{--}47\text{ M}_{\text{Jupiter}}^1$ .

Applying the same technique of S06, we derive the possible solutions in  $\log g$  and  $T_{\text{eff}}$  for 2MASS J0415–0935 and 2MASS J1217–0311, shown as curves in Figure 3. These objects' kinematics constrain their ages to be in the range 1–10 Gyr. Tables 2 and 3 give a set of specific values along each curve for  $T_{\text{eff}}$ ,  $\log g$ , luminosity, mass, radius and age for these dwarfs for both  $[\text{Fe}/\text{H}] = 0$  and  $+0.3$ . Note that the tabulated solutions have nearly constant  $L_{\text{bol}}$ . This is not an assumption of the method but a consequence of the very weak dependence of the calculated bolometric correction on  $T_{\text{eff}}$  of the atmosphere models when the bolometric flux correction is  $\lesssim 30\%$ . Our values of  $L_{\text{bol}}$  agree with those of Golimowski et al. (2004) within the quoted uncertainties for both objects. For a given object, the solutions for

---

<sup>1</sup>Table 1 of Saumon et al. (2006) gives erroneous values of  $L_{\text{bol}}$  for two of the models. The correct values are  $\log L_{\text{bol}}/L_{\odot} = -5.521$  for model A and  $-5.528$  for model C.

$[\text{Fe}/\text{H}] = 0$  and  $+0.3$  are very close to each other, which shows that this method of determination of  $(T_{\text{eff}}, g)$  is quite robust, given a good sampling of the spectral energy distribution (SED). These models are also indicated in Figure 3 for solar composition. The points chosen along each curve correspond to ages of 1 Gyr (models A & D),  $\sim 3$  Gyr (models B & E) and 10 Gyr (models C & F). Atmospheric models and synthetic spectra were generated for these parameters, and are compared to the observed spectra and photometry in §6 to determine the optimum range of parameters for each dwarf.

## 6. Comparison of Observed and Synthetic Spectra and Photometry

With the values of  $T_{\text{eff}}$  and  $g$  constrained to lie along the curves shown in Figure 3 and between the ages of 1 and 10 Gyr, we now seek to further constrain the allowed range by optimizing the fits of the corresponding synthetic spectra to the observations. For this purpose, we have three parameters at our disposal. One is the location along the solution curve, which for convenience we will parametrize with the gravity (mass, radius, age, and  $T_{\text{eff}}$  are other possible choices), the metallicity of the atmosphere, for which we consider values of  $[\text{Fe}/\text{H}] = 0$  and  $+0.3$ , and the time scale of mixing in the radiative part of the atmosphere, parametrized by the eddy diffusion coefficient with values of  $K_{zz} = 0, 10^2, 10^4$ , and  $10^6 \text{ cm}^2/\text{s}$ . Values of  $K_{zz}$  increasing from zero will give increasingly vigorous mixing and larger departures from chemical equilibrium. The introduction of vertical mixing and its associated parameter is motivated by strong evidence of departures from chemical equilibrium in late T dwarfs which can be well modelled by this process (Noll et al. 1997; Saumon et al. 2000; Golimowski et al. 2004; Saumon et al. 2006); we explore whether this is also the case for 2MASS J0415–0935 and 2MASS J1217–0311. By combining the radius,  $R(T_{\text{eff}}, g)$ , from the evolution calculations and the parallax, we compute fluxes at Earth from the models and compare them directly with the observed fluxes, without any arbitrary normalization, except where indicated otherwise.

In the following comparison of the models with the spectroscopic and photometric data, we first discuss the near-infrared spectrum, which provides the best constraint on the metallicity through the  $K$ -band peak, followed by the mid-infrared spectrum, where  $\text{NH}_3$  bands are indicators of the presence of departures from chemical equilibrium. Finally,  $3\text{--}4 \mu\text{m}$  spectroscopy and photometry provide a consistency check on the previous determinations and  $4\text{--}5 \mu\text{m}$  photometry gives a measure of the mixing time scale in the radiative region of the atmosphere through the strength of the  $4.7 \mu\text{m}$  band of CO.

## 6.1. 2MASS J0415–0935

### 6.1.1. $0.7\text{--}2.5\mu\text{m}$ spectrum

The synthetic spectra of each of the triplets of models (Table 2) are very similar to each other in the near-infrared, because the effect of increasing the gravity is partially canceled by the accompanying increase in effective temperature from models A to C. The  $(P, T)$  structures of these three models are almost identical, with deviations of less than 0.14 dex in pressure at a given temperature. The general agreement of the synthetic spectra with the data is very good (Figure 4), although there are some systematic deviations. For example, (1) the  $1.6\mu\text{m}$  band of  $\text{CH}_4$  is too weak in the models; (2) the  $J$ -band peak is too broad, and (3) the shape of the  $Y$ -band peak is incorrect. The first is due to incompleteness of the  $\text{CH}_4$  line list at temperatures above 300 K, and the other two to the absence of  $\text{CH}_4$  opacity in our model spectra below  $1.50\mu\text{m}$ . The known bands of  $\text{CH}_4$  at shorter wavelengths (Strong et al. 1993) have no corresponding line list but they are located such as to increase the opacity on both sides of the  $J$ -band peak (Figure 1), making it narrower, and to cut into the blue side of the  $Y$ -band peak. The latter may also be affected by the profile we have adopted for the far red wing of the K I resonance doublet (Burrows et al. 2000). As S06 found for Gl 570D, the solar metallicity models all underestimate the  $K$ -band flux of 2MASS J0415–0935, which suggests that it may be enriched in metals. Spectra with  $[\text{Fe}/\text{H}] = +0.3$  (models A', B', C' in Table 2) reproduce the  $K$ -band peak very well but the  $J$  peak becomes much too strong. The best synthetic near-infrared spectra are model C for  $[\text{Fe}/\text{H}] = 0$  and model C' for  $[\text{Fe}/\text{H}] = +0.3$ . As can be seen from Figure 4, neither value of the metallicity provides a better fit to the optical and near-infrared spectrum. No improvement would come from an intermediate value of  $[\text{Fe}/\text{H}]$  either. The high end of the allowed gravity range is somewhat preferred as it provides a slightly better match to the  $Y$ -band peak.

### 6.1.2. $5\text{--}15\mu\text{m}$ spectrum

The mid-infrared spectrum covers strong bands of  $\text{NH}_3$ , a tracer of non-equilibrium chemistry which can reduce the  $\text{NH}_3$  abundance in the atmosphere by a factor of  $\sim 10$  (Saumon et al. 2006). In this spectral range, the average flux level decreases noticeably as the gravity increases along the sequence of models in Table 2.

We follow the approach of S06 by computing the  $\chi^2$  between the synthetic spectra and the observed spectrum beyond  $9\mu\text{m}$  for each triplet of models, four values of  $K_{zz}$  and both metallicities. In all cases, the best non-equilibrium model ( $K_{zz} > 0$ ) provides a much better match than the best equilibrium model, at a very high level of significance ( $\gtrsim 50\sigma$ ). If we

allow for arbitrary normalization of the flux rather than considering the absolute fluxes, we find that the equilibrium abundance of  $\text{NH}_3$  is still ruled out at the  $22\sigma$  level. Therefore both the average flux level and the detailed shape of the spectrum give a  $\text{NH}_3$  abundance that is well below that predicted by equilibrium chemistry. Other explanations (e.g. low intrinsic nitrogen abundance) are ruled out in S06. For  $[\text{Fe}/\text{H}] = 0$ , the best equilibrium model ( $K_{zz} = 0$ ) is clearly A. The best non-equilibrium model is B with  $K_{zz} = 10^4 - 10^6 \text{ cm}^2 \text{ s}^{-1}$ . These spectra are shown in Figure 5. For  $[\text{Fe}/\text{H}] = +0.3$ , model A' is the best equilibrium model and the best match with non-equilibrium chemistry is obtained with model C' and  $K_{zz} = 10^6 \text{ cm}^2 \text{ s}^{-1}$ . Non-equilibrium, solar metallicity models give significantly better fits, however.

#### 6.1.3. $2.9\text{--}4.1\mu\text{m}$ spectrum

The  $3\text{--}4\mu\text{m}$  spectrum shows a very strong and very broad  $3.3\mu\text{m}$   $\text{CH}_4$  band, which is saturated at the center (Figure 6). Only the  $3.9 - 4.1\mu\text{m}$  region is sensitive to the  $\text{CH}_4$  abundance, which depends on the metallicity and potential departures from chemical equilibrium. The latter act to reduce the  $\text{CH}_4$  abundance in the upper atmosphere. The three solar metallicity models reproduce the spectrum well but underestimate the  $3\mu\text{m}$  bump by about  $2\sigma$ . Non-equilibrium chemistry raises the flux in the  $3\mu\text{m}$  bump and brings it in excellent agreement with the data (Figure 6). It also raises the flux longward of  $3.9\mu\text{m}$  to a level generally higher than the data, but within the  $1\sigma$  error bars. The metal-rich model spectra are quite similar but their higher abundance of  $\text{CH}_4$  results in somewhat lower fluxes in the  $3.9\text{--}4.1\mu\text{m}$  region than those of the solar metallicity spectra. This can be compensated by a higher value of  $K_{zz}$ , however. The  $2.9\text{--}4.1\mu\text{m}$  spectrum has  $\text{SNR} \sim 6 - 7$ , which is not sufficient to discriminate between our different model spectra. All of them are in fair agreement with the data; non-equilibrium models (with any  $K_{zz}$ ) fit the  $3\mu\text{m}$  bump better, however.

#### 6.1.4. Photometry

Figure 7 shows the synthetic photometry in the MKO  $L'$  and  $M'$  bands and the IRAC bands [3.55] and [4.49], along with the observed values. The  $M'$  and [4.49] bands both probe the  $4.7\mu\text{m}$  band of CO, a sensitive tracer of non-equilibrium chemistry, which can dramatically enhance the CO abundance (Figure 6).

The synthetic  $L'$  magnitude is a weak function of gravity, metallicity and  $K_{zz}$ , with all

models giving values that agree to within  $\pm 0.25$  magnitude. With solar metallicity models, the  $L'$  magnitude is best reproduced with models A and B with  $K_{zz} = 0$  and increasing  $K_{zz}$  drives the synthetic  $L'$  steadily away from the observed values. At  $[\text{Fe}/\text{H}] = +0.3$ , all three models provide a good match for  $K_{zz} \sim 10 - 10^4 \text{ cm}^2 \text{ s}^{-1}$ . The MKO  $L'$  filter measures the  $3.45 - 4.1 \mu\text{m}$  flux and discriminates better between the various models than our  $2.9 - 4.1 \mu\text{m}$  spectrum.

Not surprisingly, the IRAC [3.55] magnitude behaves very much like  $L'$  but models generally are fainter than the observed value. The latter can only be reproduced with model C (any  $K_{zz}$ ) or with any model (including both metallicities) if  $K_{zz} \sim 10^6 \text{ cm}^2 \text{ s}^{-1}$ .

The MKO  $M'$  and IRAC [4.49] magnitudes behave similarly and give a consistent picture where  $K_{zz} = 0$  is strongly excluded and good matches can be obtained for any gravity if  $K_{zz} \sim 10^5 - 10^6 \text{ cm}^2 \text{ s}^{-1}$  (solar metallicity) or  $K_{zz} \sim 10^3 - 10^4 \text{ cm}^2 \text{ s}^{-1}$  ( $[\text{Fe}/\text{H}] = +0.3$ ). This is strong evidence that the  $4.7 \mu\text{m}$  band of CO is deep in 2MASS J0415–0935 and that the CO abundance is well above the chemical equilibrium value (Figure 6).

#### 6.1.5. Optimum models

No single synthetic spectrum fits this extensive data set but a clear picture emerges. The IRS spectrum, and the  $M'$  and [4.49] magnitudes all clearly indicate that  $\text{NH}_3$  is under abundant and CO is overabundant compared to the values expected from chemical equilibrium. In 2MASS J0415–0935, the chemistry of nitrogen is quenched in the convection zone where the mixing time scale is determined by the mixing length theory of convection. The  $\text{NH}_3$  bands in the IRS spectrum are therefore good indicators of the presence of non-equilibrium chemistry but do not provide a handle on the value of the mixing time scale parameter in the radiative zone,  $K_{zz}$ . On the other hand, the carbon chemistry is quenched in the radiative zone and is quite sensitive to  $K_{zz}$ .

In this analysis, we are not able to determine the metallicity of 2MASS J0415–0935. Both  $[\text{Fe}/\text{H}] = 0$  and  $[\text{Fe}/\text{H}] = +0.3$  can give equally good agreements with each segment of spectrum and each magnitude (with different parameters, however). Overall, most aspects of the SED can be reproduced fairly well by models in the range between models B and C (or  $B'$  and  $C'$  for  $[\text{Fe}/\text{H}] = +0.3$ ) with a coefficient of eddy diffusion of  $K_{zz} \gtrsim 10^4 \text{ cm}^2 \text{ s}^{-1}$ . The parameters of 2MASS J0415–0935 are thus:  $T_{\text{eff}} = 725 - 775 \text{ K}$ ,  $\log g = 5.00 - 5.37$ ,  $\log L_{\text{bol}}/L_{\odot} = -5.67$ ,  $M = 33 - 58 M_{\text{Jupiter}}$ , and age between 3 and 10 Gyr. This range of parameters is highlighted in Figure 3. An example of such a model is shown in Figure 8 and its corresponding synthetic magnitudes are shown in Figure 7. 2MASS J0415–0935 is

the least luminous T dwarf analyzed in details so far and is also the coolest (Figure 3). In comparison, the  $T_{\text{eff}}$  and  $\log g$  derived by Burgasser et al. (2006b) (their Figure 9) is about 40 K hotter than ours for their quoted range of gravity ( $\log g = 4.9\text{--}5.0$ ). Their parameters correspond to  $\log L_{\text{bol}}/L_{\odot} = -5.59 \pm 0.02$ , which is consistent with our model B within their quoted uncertainties.

## 6.2. 2MASS J1217–0311

### 6.2.1. $0.7\text{--}2.5\mu\text{m}$ spectrum

For 2MASS J1217–0311 the near-infrared model spectra for both metallicities again give very nearly identical solutions for  $L_{\text{bol}}$ ,  $T_{\text{eff}}$  and  $\log g$  (Table 3). And again, we find that the solar metallicity models underestimate the  $K$ -band flux significantly, although the agreement with the  $Y$  and  $J$  peaks is excellent (Figure 9). On the other hand, models with  $[\text{Fe}/\text{H}] = +0.3$  give an excellent fit of the entire near-infrared SED, except for the usual problem with the  $1.6\mu\text{m}$  band of  $\text{CH}_4$ . The maximum  $J$ -band flux is less sensitive to  $[\text{Fe}/\text{H}]$  at the higher  $T_{\text{eff}}$  of 2MASS J1217–0311 than it is for 2MASS J0415–0935, allowing a good fit of the  $K$ -band peak at  $[\text{Fe}/\text{H}] = +0.3$  without compromising the good fit of the  $J$ -band peak. The width of the  $J$ -band peak is also much better reproduced than for 2MASS J0415–0935 because the temperature where it is formed in the atmosphere is higher and the  $\text{CH}_4$  contribution to the opacity smaller than in 2MASS J0415–0935. Water is now mostly responsible for shaping the  $J$ -band peak and the omission of  $\text{CH}_4$  opacity in this wavelength range (§6.1.1) is of lesser consequence. The best fitting models with  $[\text{Fe}/\text{H}] = 0$  and  $+0.3$  are shown in Figure 9. The quality of the fit with  $[\text{Fe}/\text{H}] = +0.3$  suggests that 2MASS J1217–0311 is likely a metal-rich brown dwarf.

### 6.2.2. $5\text{--}15\mu\text{m}$ spectrum

The goodness of fit of the models to the IRS spectrum of 2MASS J1217–0311, as measured by their  $\chi^2$ , shows no statistically significant sensitivity to the choice of gravity or to the value of the coefficient of eddy diffusion,  $K_{zz}$ . It is not possible to distinguish between the solar metallicity models D, E and F, or between the metal-rich models D', E', and F' (Table 3), or to determine whether the chemistry departs from strict equilibrium ( $K_{zz} = 0$ ). This is largely due to the lower signal-to-noise ratio of the spectrum, which ranges from 3 to 12 for  $\lambda \geq 9\mu\text{m}$ , compared to  $\sim 9$  to 54 for the IRS spectrum of 2MASS J0415–0935. Since the near-infrared spectrum strongly favors a metal-rich composition ( $[\text{Fe}/\text{H}] = +0.3$ ), we show

in Figure 10 the best fitting metal-rich equilibrium model (model E' with  $K_{zz} = 0$ ) and the best fitting non-equilibrium model (model F') with  $K_{zz}$  arbitrarily set to  $100 \text{ cm}^2 \text{ s}^{-1}$  since the  $\chi^2$  doesn't vary with  $K_{zz}$  in this case. The slope of the spectrum beyond  $11 \mu\text{m}$  appears to be steeper than in the models, which accounts partly for the inability to select among the various models considered on the basis of the  $\chi^2$ . The  $4.7 \mu\text{m}$  band of CO is predicted to be quite strong even for such a modest value of  $K_{zz}$ .

### 6.2.3. Photometry

In Figure 11, the MKO  $L'$  and the IRAC [3.55] and [4.49] magnitudes of 2MASS J1217–0311 are compared to the synthetic magnitudes for all six models in Table 3, as the coefficient of eddy diffusion is varied from  $K_{zz} = 0$  to  $10^6 \text{ cm}^2 \text{ s}^{-1}$ . The metal-rich models generally fare better in all three bands. The  $L'$  magnitude favors low values of  $K_{zz} \lesssim 10^2 \text{ cm}^2 \text{ s}^{-1}$ , while the IRAC [3.55] band is a rather poor match unless  $K_{zz}$  is high ( $\sim 10^6 \text{ cm}^2 \text{ s}^{-1}$ ). The IRAC [4.49] band, which measures the non-equilibrium tracer CO, favors non-equilibrium models with  $K_{zz} \gtrsim 10^2 \text{ cm}^2 \text{ s}^{-1}$  and more likely  $\gtrsim 10^4 \text{ cm}^2 \text{ s}^{-1}$ . We cannot get a consistent fit for these three magnitudes, however, which most likely reflects a limitation of our models.

### 6.2.4. Optimum models

The near-infrared spectrum of 2MASS J1217–0311 indicates that it is metal-rich, with  $[\text{Fe}/\text{H}]$  close to  $+0.3$ , which is consistent with the photometry shown in Figure 11. While the IRS spectrum shows prominent bands of  $\text{NH}_3$ , it is too noisy to indicate whether the  $\text{NH}_3$  abundance departs from chemical equilibrium or even to constrain the gravity. The full range of  $T_{\text{eff}}$  and  $\log g$  of models D', E', and F' (Table 3 and highlighted in Figure 3) remains plausible. Evidence for non-equilibrium chemistry comes solely from the IRAC [4.49] magnitude, which is 0.2 to 0.4 mag below that expected from chemical equilibrium.

To summarize, 2MASS J1217–0311 has  $[\text{Fe}/\text{H}] \sim +0.3$ ,  $T_{\text{eff}} = 850$  to  $950 \text{ K}$ ,  $\log g = 4.80$  to  $5.42$ ,  $\log L_{\text{bol}}/L_{\odot} = -5.31$ , and we are unable to constrain the age to better than  $1$ – $10 \text{ Gyr}$ . This implies a mass between  $25$  and  $65 M_{\text{Jupiter}}$ . The values derived by Burgasser et al. (2006b) agree with our model D' at the  $1\sigma$  level, based on their quoted uncertainty. On the basis of the IRAC [4.49] magnitude, it appears that CO is more abundant than expected from chemical equilibrium and that a coefficient of eddy diffusion  $K_{zz} \gtrsim 10^2 \text{ cm}^2 \text{ s}^{-1}$  (possibly as high as  $10^6 \text{ cm}^2 \text{ s}^{-1}$ ) is appropriate to model this object. A model that represents a good compromise between all the constraints (model E' in Table 3, with  $K_{zz} = 10^2 \text{ cm}^2 \text{ s}^{-1}$ )

is compared to the spectrum in Figure 12 and the corresponding photometry is shown in Figure 11.

## 7. Conclusions

The new 3–4  $\mu\text{m}$  and 5–15  $\mu\text{m}$  spectra presented here for the T8 dwarf 2MASS J0415–0935, together with its near-infrared spectrum and trigonometric parallax, allow a very accurate determination of its bolometric luminosity ( $\log L_{\text{bol}}/L_{\odot} = -5.67 \pm 0.02$ ) and constrain the possible values of  $(T_{\text{eff}}, g)$ . Although the age for this isolated disk dwarf is not known, comparisons of synthetic to observed red through mid-infrared spectra show that we can constrain it to 3–10 Gyr, with corresponding values of  $T_{\text{eff}} = 725\text{--}775\text{ K}$ ,  $\log g = 5.00\text{--}5.37$  and a mass between 33 and  $58 M_{\text{Jupiter}}$ . These ranges are different from error bars in the sense that the values of  $T_{\text{eff}}$ ,  $\log g$  and  $M$  within the quoted intervals are correlated (Figure 3 and Table 2). The metallicity is likely between  $[\text{Fe}/\text{H}] = 0$  and  $+0.3$ .

Applying the same method of analysis, using published data, to the T7.5 dwarf 2MASS J1217–0311, we find  $\log L_{\text{bol}}/L_{\odot} = -5.31 \pm 0.03$  and an age of 1–10 Gyr. These correspond to  $T_{\text{eff}} = 850\text{--}950\text{ K}$ ,  $\log g = 4.80\text{--}5.42$  and a mass of 25 to  $65 M_{\text{Jupiter}}$ . The metallicity of 2MASS J1217–0311 is  $[\text{Fe}/\text{H}] \sim +0.3$ , which indicates that it is very unlikely to be as old as 10 Gyr. The lower end of each of the parameter ranges given above is therefore more appropriate.

In terms of  $T_{\text{eff}}$ , 2MASS J1217–0311 and 2MASS J0415–0935 straddle the value of 800–820 K derived for the T7.5 dwarf Gl 570D by S06. The spectral classifications are uncertain by half a subclass, but on face value the half subclass difference between Gl 570D and 2MASS J0415–0935 corresponds to a  $\sim 60$  K difference in  $T_{\text{eff}}$  if both objects have the same gravity (Figure 3). Although 2MASS J1217–0311 has the same spectral type as Gl 570D, it is warmer by 30–170 K, depending on the respective gravity of each object. At the low end, this difference is not significant but a higher value would warrant a study of the effects of gravity and metallicity on the indices used to determine the spectral type of T dwarfs (Burgasser et al. 2006a).

As was found previously for Gl 229B (Noll et al. 1997; Oppenheimer et al. 1998; Saumon et al. 2000) and Gl 570D (Saumon et al. 2006), we find evidence for departures from equilibrium chemistry in both objects studied here. Specifically, the mid-infrared band of  $\text{NH}_3$  in 2MASS J0415–0935 is weaker than expected from chemical equilibrium models. The IRS spectrum can be fit very well if the  $\text{NH}_3$  abundance is decreased by a factor of 8–10. The MKO  $M'$  magnitude of 2MASS J0415–0935 is  $\sim 1$  magnitude fainter than equi-

librium models predict, a clear indication of a significant enhancement of the CO abundance. Similarly, the IRAC [4.55] magnitude of 2MASS J1217–0311 is 0.2 to 0.4 magnitude fainter than expected, showing a more modest enhancement of CO than in 2MASS J0415–0935, compared to the predictions of equilibrium models.

Departures of the chemistry of carbon and nitrogen from chemical equilibrium is the consequence of a simple mechanism based on the kinetics of the relevant chemical reactions and the assumption that vertical mixing takes place. Unless the radiative zone is quiescent on time scales of years, non-equilibrium chemistry of carbon and nitrogen should be a common feature to all low- $T_{\text{eff}}$  brown dwarfs. These departures from chemical equilibrium can be modelled by considering vertical mixing in the atmosphere and the time scales of the reactions that are responsible for the chemistry of nitrogen and carbon. Deep in the atmosphere, the mixing time scale is determined by the properties of the convection zone, modelled with the mixing length theory. In the radiative zone, mixing is caused by some undetermined physical process on a longer, and a priori unknown, time scale. This time scale is the only free parameter of the non-equilibrium models. Until the physical processes that can cause mixing in the radiative zone of brown dwarf atmospheres are modelled, we have no indication as to the value of that mixing time scale. Fegley & Lodders (1994) show that the non-equilibrium abundances of CO, HCN, GeH<sub>4</sub>, AsH<sub>3</sub> and PH<sub>3</sub> observed in Jupiter and Saturn can all be modelled very well with  $K_{zz} = 10^7$  to  $10^9 \text{ cm}^2 \text{ s}^{-1}$ . However, all of these species are quenched deep in the convection zone, which is consistent with the high values of  $K_{zz}$  needed to reproduce their abundances.<sup>2</sup> The value of  $K_{zz}$  in the radiative zones of brown dwarf atmospheres thus remains unconstrained, except for an upper limit provided by the mixing time scale in the convection zone. In this context, the successful modeling of the spectra of brown dwarfs with a simple, one parameter model may provide guidance in determining the physical process(es) responsible for the mixing. As more objects are analyzed in detail, a pattern may emerge in the derived values of  $K_{zz}$  that can be compared with the results of detailed modeling of mixing processes when it becomes available. The mixing time scale parametrized by  $K_{zz}$  also enters the modeling of clouds in L dwarfs (Ackerman & Marley 2001), and empirically determined values of  $K_{zz}$  in brown dwarfs allows for the development of a more consistent theory of vertical mixing and of the cloud model.

Of the four brown dwarfs that have been studied in enough detail so far, three show clear evidence of non-equilibrium abundances for at least one of the two key tracers (NH<sub>3</sub> and CO):

---

<sup>2</sup>In our models,  $K_{zz}$  is used to parametrize the mixing time scale in the radiative zone only and the mixing time scale in the convection zone is computed with the mixing length theory. In the planetary science literature,  $K_{zz}$  is used to parametrize the mixing time scale regardless of whether the mixing occurs in a radiative or a convective zone.

Gl 229B, Gl 570D and 2MASS J0415–0935. The fourth, 2MASS J1217–0311 appears to have a non-equilibrium CO abundance. In all four objects, the nitrogen chemistry is quenched in the convection zone, where the mixing time scale is not adjustable. The depletion of  $\text{NH}_3$  that ensues depends very weakly on the value of  $K_{zz}$ . On the other hand, their carbon chemistry is quenched in the radiative zone, and the flux in the  $4.7\text{ }\mu\text{m}$  band of CO is very sensitive to the choice of  $K_{zz}$ . The values found so far for the coefficient of eddy diffusivity in the radiative zone are  $\log K_{zz} = 4–5$  for Gl 229B (based on the CO mole fraction determined by Saumon et al. (2000)), and  $\sim 5–6$  for 2MASS J0415–0935. For 2MASS J1217–0311, the three photometric measurements cannot be fit simultaneously and we find a weak constraint of  $\log K_{zz} > 2$ . If we (arbitrarily) ignore its  $L'$  magnitude, then  $\log K_{zz} \gtrsim 5$  gives a very good fit to all the other data.

The present analysis of 2MASS J0415–0935 and of 2MASS J12170311 is based on fits of the low-resolution SED. Medium resolving power ( $\lambda/\Delta\lambda \gtrsim 2000$ ) and especially high resolving power ( $\lambda/\Delta\lambda \gtrsim 20000$ ) near-infrared spectra open the possibility of constraining the gravity by fitting the fine structure of the spectrum, which should further limit the ranges of  $T_{\text{eff}}$  and  $\log g$  obtained here as well as the value of  $K_{zz}$ . Such an analysis will be greatly simplified by the fact that the fitted model must lie on the curves shown in Figure 3, which reduces the fit from a three-dimensional parameter space ( $T_{\text{eff}}, \log g, [\text{Fe}/\text{H}]$ ) to a two-dimensional space ( $\log g, [\text{Fe}/\text{H}]$ ).

This work is based in part on data collected at the Subaru Telescope, which is operated by the National Astronomical Observatory of Japan. This work is also based in part on observations made with the *Spitzer Space Telescope*, which is operated by the Jet Propulsion Laboratory, California Institute of Technology under a contract with NASA. Support for this work was provided by NASA through an award issued by JPL/Caltech. This work was also supported in part under the auspices of the U.S. Department of Energy at Los Alamos National Laboratory under Contract W-7405-ENG-36. MCC acknowledges support from NASA through the Spitzer Space Telescope Fellowship Program, through a contract issued by JPL/Caltech. Work by KL is supported by NSF grant AST-0406963. MSM acknowledges the support of the NASA Office of Space Sciences. TRG and SKL are supported by the Gemini Observatory, which is operated by the Association of Universities for Research in Astronomy Inc. (AURA), under a cooperative agreement with the NSF on behalf of the Gemini partnership: the National Science Foundation (United States), the Particle Physics and Astronomy Research Council (United Kingdom), the National Research Council (Canada), CONICYT (Chile), the Australian Research Council, CNPq (Brazil) and CONICET (Argentina).

## REFERENCES

Ackerman, A. S. & Marley, M. S. 2001, *ApJ*, 556, 872

Beichman, C. A., Chester, T. J., Skrutskie, M., Low, F. J. & Gillett, F. 1998, *PASP*, 110, 480

Bézard, B., Lellouch, E., Strobel, D., Maillard, J.-P., & Drossart, P. 2002, *Icarus*, 159, 95

Burgasser, A. J. et al. 1999, *ApJ*, 522, L65

Burgasser, A. J. et al. 2000, *ApJ*, 531, L57

Burgasser, A. J. et al. 2002, *ApJ*, 564, 421

Burgasser, A. J., Kirkpatrick, J. D., Liebert, J. & Burrows, A. 2003, *ApJ*, 594, 510

Burgasser, A. J., Geballe, T. R., Leggett, S. K., Kirkpatrick, J. Davy & Golimowski, D. A. 2006, *ApJ*, 637, 1067

Burgasser, A. J., Burrows, A. & Kirkpatrick, J. D. 2006, *ApJ*, 639, 1095

Burgasser, A. J. 2006, *ApJ*, submitted

Burrows, A., Marley, M. S. & Sharp, C. M. 2000, *ApJ*, 531, 438

Burrows A., Hubbard W. B., Lunine, J. I. & Liebert, J. 2001, *Reviews of Modern Physics*, 73, 719 & Lunine, J.. I. 2003, *ApJ*, 596, 587

Cushing, M. C., Vacca, W. D. & Rayner, J. T. 2004, *PASP*, 116, 362

Cushing, M. C. et al. 2006, *ApJ*, 648, 614

Eggen O.J. 1998, *AJ*, 115, 2397

ESA 1997, The Hipparcos and Tycho Catalogues (ESA SP-1200) (Noordwijk: ESA)

Fazio, G. et al., 2004, *ApJS*, 154, 10

Fegley, B. Jr. & Lodders, K. 1994, *Icarus*, 110, 117

Fegley, B. Jr. & Lodders, K. 1996, *ApJ*, 472, L37

Geballe, T. R., Saumon, D., Leggett, S. K., Knapp, G. R., Marley, M. S. & Lodders, K. 2001, *ApJ*, 556, 373

Geballe, T. R. et al. 2002, *ApJ*, 564, 466

Golimowski D. A. et al. 2004, *AJ*, 127, 3516

Griffith, C. A. & Yelle, R. V. 1999, *ApJ*, 519, L85

Higdon, S. J. U. et al. 2004, *PASP*, 116, 975

Houck, J. et al. 2004, *ApJS*, 154, 18

Knapp, G. R. et al. 2004, *AJ*, 127, 3553

Kobayashi, N., et al. 2000, Proc. SPIE 4008: Optical and IR Telescope Instrumentation and Detectors, eds M. Iye & A. F. Moorwood, 1056

Leggett, S. K. et al. 2002, *ApJ*, 564, 452

Lodders, K. 2003, *ApJ*, 591, 1220

Lodders, K. & Fegley, B. Jr. 2002, *Icarus*, 155, 393

Luhman, K. L. et al. 2006, *ApJ*, in press

Liu, M. C., Leggett, S. K. & Chiu, K. 2006, *ApJ*, submitted

Mugrauer, M., Seifahrt, A., Neuhaeuser, R. & Mazeh, T. 2006, *MNRAS* in press

Noll, K. S., Geballe, T. R. & Marley, M. S. 1997, *ApJ*, 489, L87

Oppenheimer, B. O., Kulkarni, S. R., Matthews, K. & van Kerkwijk, M. H. 1998, *ApJ*, 502, 932

Patten, B. M., et al. 2006, *ApJ*, in press

Prinn, R. G. & Barshay, S. S. 1977, *Science*, 198, 1031

Saumon, D., Geballe, T. R., Leggett, S. K., Marley, M. S., Freedman, R. S., Lodders, K., Fegley, B. Jr. & Sengupta, S. K. 2000, *ApJ*, 541, 374

Saumon, D., Marley, M. S., Cushing, M. C., Leggett, S. K., Roellig, T. L., Lodders, K. & Freedman, R. S. 2006, *ApJ*, 647, 552 (S06)

Saumon, D., Marley, M. S. , Lodders, K. & Freedman, R. S. 2003, in Brown Dwarfs, IAU Symp. 211, E.L. Martín, Ed., (ASP: San Francisco), 335

Skrutskie, M. F. et al. 2006, *AJ*, 131, 1163

Strong, K., Taylor, F. W., Calcutt, S. B., Remedios, J. J. & Ballard, J. 1993,  
J. Quant. Spec. Radiat. Transf., 60, 665

Tinney, C. G., Burgasser, A. J. & Kirkpatrick, J. D. 2003, AJ, 126, 975

Tinney, C. G., Burgasser, A. J., Kirkpatrick, J. D. & McElwain, M. W. 2005, AJ, 130, 2326

Tokunaga, A. T., Simons, D. A. & Vacca, W. D. 2002, PASP, 114, 180

van Altena, W. F., Lee, J. T. & Hoffleit, E. D. 1995, The General Catalogue of Trigonometric  
Stellar Parallaxes (4th ed.; New Haven; Yale Univ. Obs.)

Vrba, F. J. et al. 2004, AJ, 127, 2948

Werner, M., et al. 2004, ApJS, 154, 1

York, D. G. et al. 2000, AJ, 120, 1579

Table 1. Published Astrometric and Photospheric Data for the T7.5–T8 Dwarfs with Measured Parallax

Name	Spectral Type <sup>a</sup>	Parallax (error)(mas)	$V_{\tan}$ (error) (km s <sup>-1</sup> )	$\log(L_{\text{bol}}/L_{\odot})$ (error) <sup>b</sup>	$T_{\text{eff}}$ (K)		$\log g$ (cm/s <sup>2</sup> )		References <sup>f</sup>	
					Spec. <sup>c</sup>	Lum. <sup>d</sup>	Spec. <sup>c</sup>	Col./Lum. <sup>e</sup>	Disc.	Astr.
HD 3651B	T7.5	90.03(0.72)	31.0(1.2)	-5.60(0.05)	760-920	780-840	4.7-5.1	5.1-5.5	1,2	3
2MASS J04151954–0935066	T8	174.34(2.76)	61.4(1.0)	-5.73(0.05)	740-760	600-750	4.9-5.0	5.0±0.25	4	5
2MASS J12171110-0311131	T7.5	93.2(2.06)	53.5(1.2)	-5.32(0.05)	860-880	725-975	4.7-4.9	4.5±0.25	6	5,7
2MASS J14571496–2121477(Gl 570D)	T7.5	170.16(1.45)	56.4(0.9)	-5.53(0.05)	780-820	800-820	5.1	5.09-5.23	8	3,9

<sup>a</sup> Spectral types are based on the near-infrared classification scheme for T dwarfs by Burgasser et al. (2006).

<sup>b</sup> Bolometric luminosities from Golimowski et al. (2004) and Luhman et al. (2006)

<sup>c</sup> Derived from the near-infrared spectral ratio technique of Burgasser, Burrows & Kirkpatrick (2006), Burgasser (2006).

<sup>d</sup> Derived from observed luminosity by Golimowski et al. (2004); Liu et al. (2006) and S06.

<sup>e</sup> Derived from near-infrared colors by Knapp et al. (2004), or from luminosity by Liu et al. (2006) and S06.

<sup>f</sup>(1) Mugrauer et al. (2006); (2) Luhman et al. (2006); (3) ESA (1997) (4) Burgasser et al. (2002); (5) Vrba et al. (2004); (6) Burgasser et al. (1999); (7) Tinney et al. (2003); (8) Burgasser et al. (2000); (9) van Altena, Lee & Hoffleit (1995).

Table 2. Range of Physical Parameters<sup>a</sup> of 2MASS J0415–0935

Model	$T_{\text{eff}}$ (K)	$\log g$ (cm/s <sup>2</sup> )	$\log(L_{\text{bol}}/L_{\odot})$	Mass (M <sub>J</sub> )	Radius (R <sub>⊕</sub> )	Age (Gyr)
[Fe/H]=0						
A	690	4.68	−5.66	19.5	0.104	1
B	730	5.04	−5.67	34.6	0.091	3.2
C	775	5.37	−5.68	57.9	0.080	10
[Fe/H]=+0.3						
A'	685	4.63	−5.66	18.3	0.106	1
B'	725	5.00	−5.67	33.4	0.093	3.2
C'	767	5.34	−5.68	55.6	0.082	10

<sup>a</sup>Uncertainties are  $\pm 0.02$  dex in  $L_{\text{bol}}$ , which translates to  $\pm 9$  K in  $T_{\text{eff}}$  (at fixed  $g$ ) and  $\pm 0.07$  dex on  $\log g$  (at fixed  $T_{\text{eff}}$ , or  $\pm 0.01$  dex at a fixed age).

Table 3. Range of Physical Parameters<sup>a</sup> of 2MASS J1217–0311

Model	$T_{\text{eff}}$ (K)	$\log g$ (cm/s <sup>2</sup> )	$\log(L_{\text{bol}}/L_{\odot})$	Mass (M <sub>J</sub> )	Radius (R <sub>⊕</sub> )	Age (Gyr)
[Fe/H]=0						
D	860	4.84	−5.30	26.4	0.100	1
E	910	5.14	−5.31	42.2	0.089	2.7
F	965	5.44	−5.31	66.2	0.079	10
[Fe/H]=+0.3						
D'	850	4.80	−5.31	25.3	0.102	1
E'	910	5.17	−5.31	44.7	0.089	3.2
F'	950	5.42	−5.32	65.3	0.080	10

<sup>a</sup>Uncertainties are  $\pm 0.03$  dex in  $L_{\text{bol}}$ , which translates to  $\sim \pm 25$  K in  $T_{\text{eff}}$  (at fixed  $g$ ) and  $\pm 0.09$  dex on  $\log g$  (at fixed  $T_{\text{eff}}$ , or  $\pm 0.03$  dex at a fixed age).

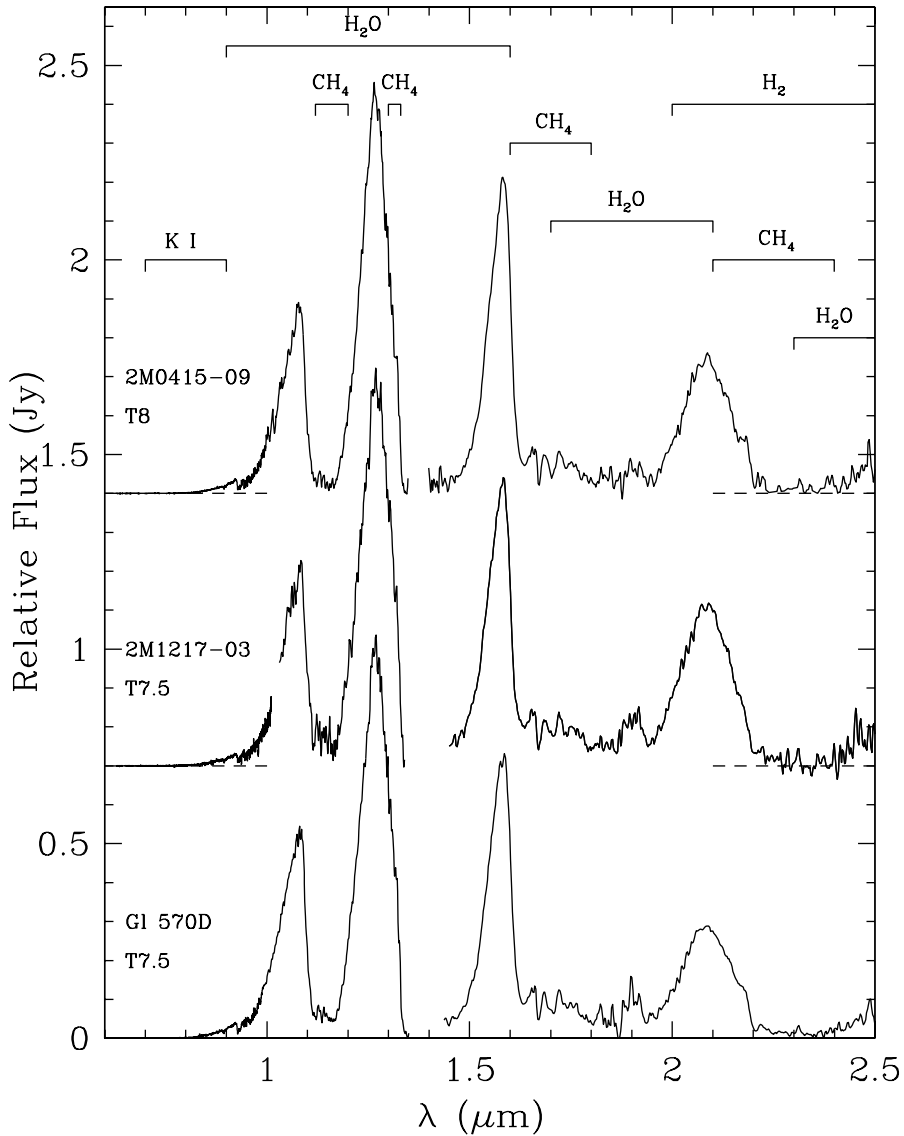


Fig. 1.— Ground-based red and near-infrared spectra of three of the six known T dwarfs later than T7: 2MASS J0415–0935, 2MASS J1217–0311 and Gl 570D. Broad and strong absorption features are identified. The spectra are normalized to the peak flux and offset, dashed lines indicate the zero flux level. Data sources are Burgasser et al. (2003), Geballe et al. (2001, 2002), and Knapp et al. (2004).

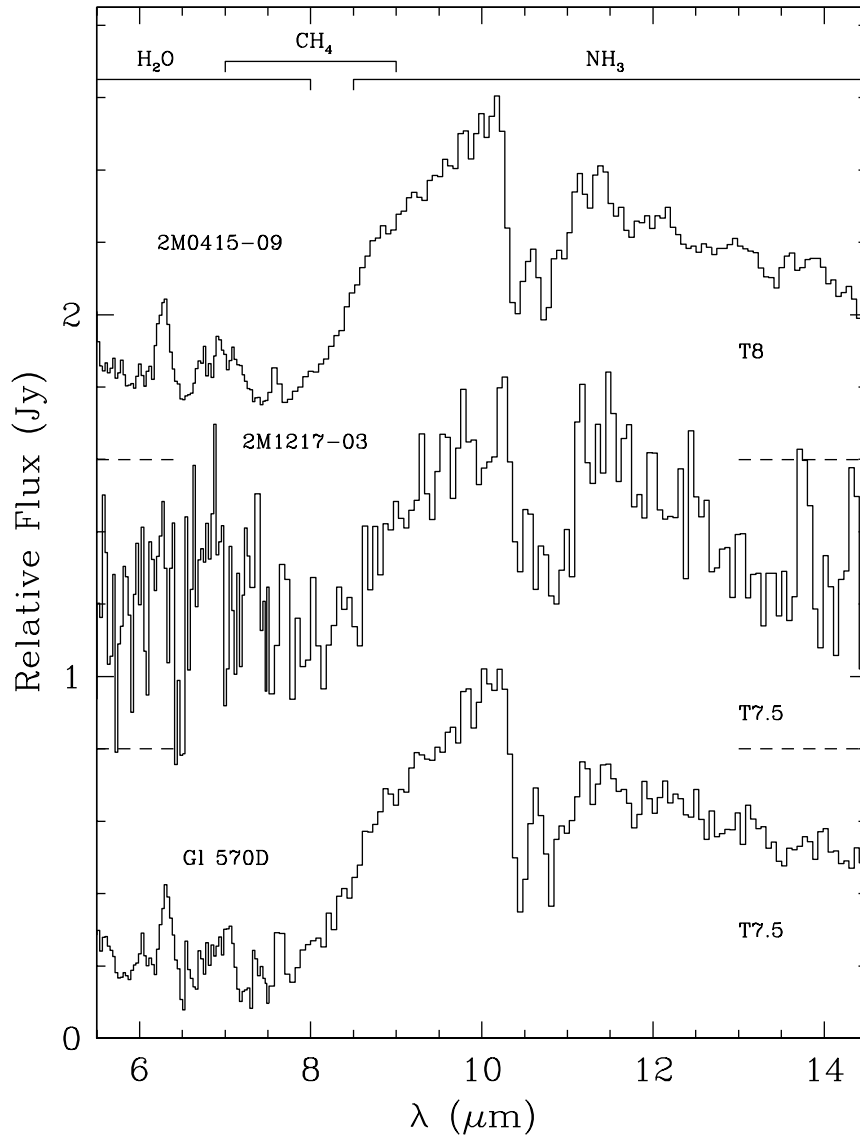


Fig. 2.— *Spitzer* IRS spectra of 2MASS J0415–0935, 2MASS J1217–0311 and Gl 570D. Broad and strong absorption features are identified. The spectra are normalized to the peak flux and offset, dashed lines indicate the zero flux level. Data sources are Cushing et al. (2006), S06 and this work.

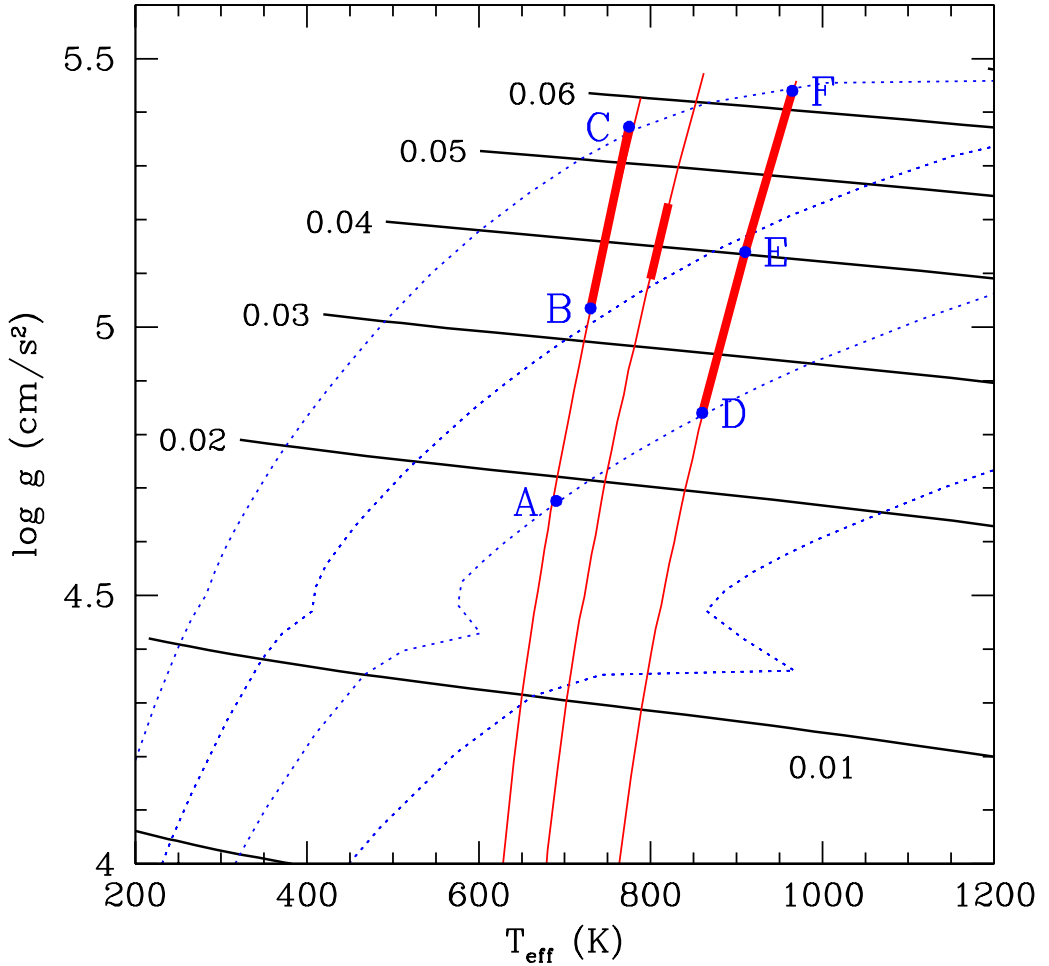


Fig. 3.— Plot of effective temperature vs. surface gravity showing brown dwarf evolution with  $[\text{Fe}/\text{H}] = 0$ . The allowed  $(T_{\text{eff}}, \log g)$  values for 2MASS J0415–0935, Gl 570D, and 2MASS J1217–0311 fall along the nearly vertical red lines from left to right, respectively.  $L_{\text{bol}}$  is very nearly constant along each curve. The heavy portion of each curve shows the restricted range of the most likely solutions based on considerations of age and fitting the spectrum and photometry of each object. Our brown dwarf evolutionary tracks are shown by thick black lines labeled with the mass in  $M_{\odot}$ . Blue dotted lines are isochrones for 0.3, 1, 3 and 10 Gyr (from right to left). Filled blue circles show the three models for 2MASS J0415–0935 and the three models for 2MASS J1217–0311 specified in Tables 2 and 3. [See the electronic edition of the Journal for a color version of this figure.]

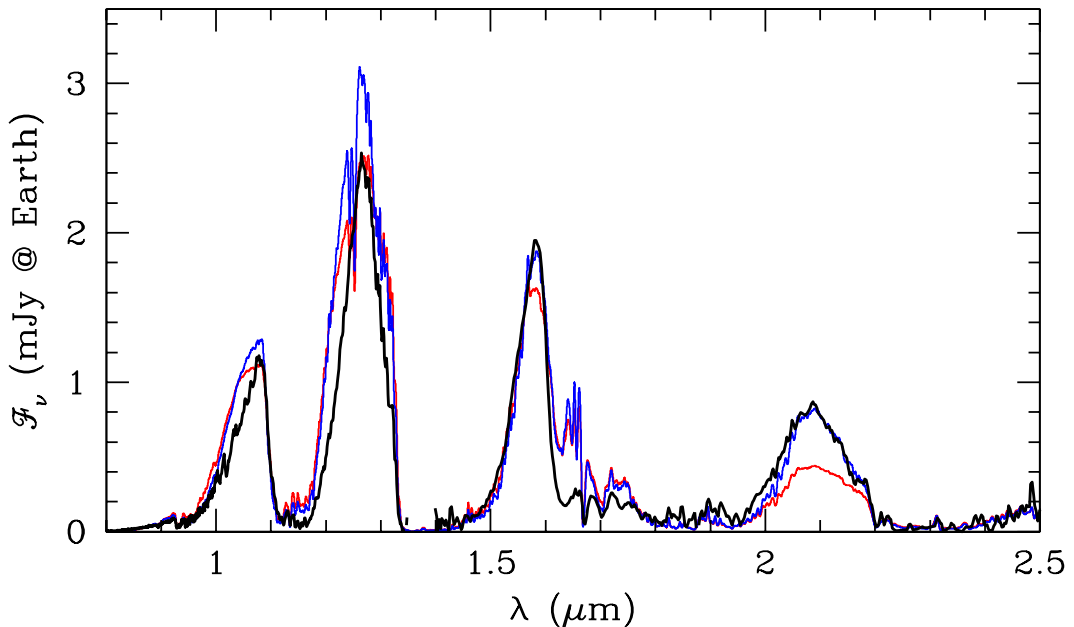


Fig. 4.— Comparison of the optical through near-infrared spectrum of 2MASS J0415–0935 with models of different metallicities. The red curve (lower thin line) is the best fitting model with  $[\text{Fe}/\text{H}] = 0$  (model C) and the blue curve (upper thin line) is the best fitting model with  $[\text{Fe}/\text{H}] = +0.3$  (model C'). Both models assume chemical equilibrium ( $K_{zz} = 0$ ). The model fluxes have not been normalized to the data but have been smoothed to a resolving power of  $\lambda/\Delta\lambda = 500$  to approximate that of the data. The data is shown by the heavy black line. [See the electronic edition of the Journal for a color version of this figure.]

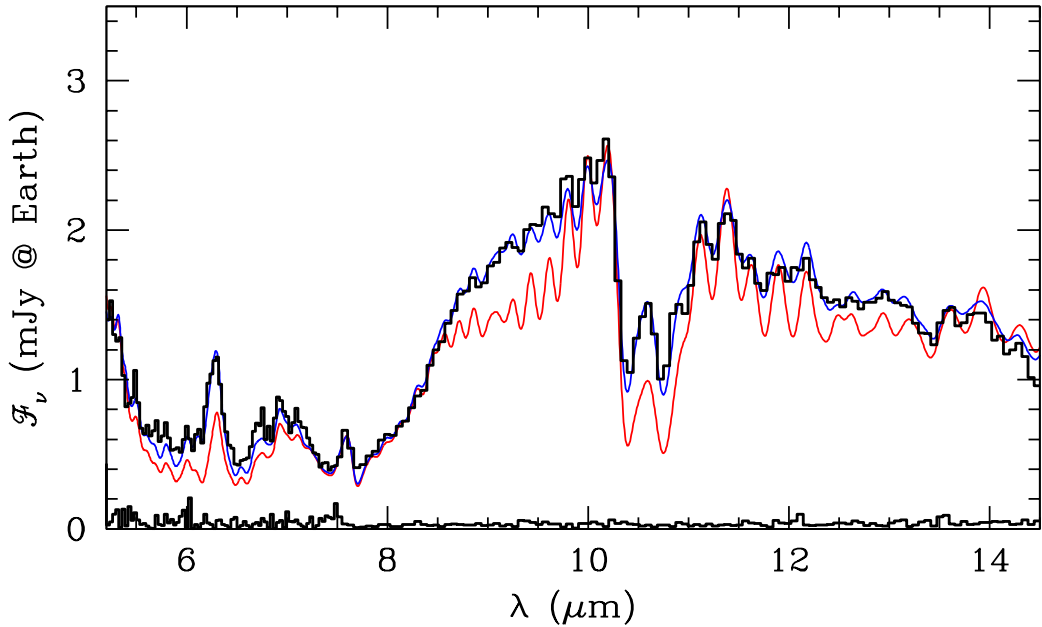


Fig. 5.— Fits of the IRS spectrum of 2MASS J0415–0935 showing the difference between a model in chemical equilibrium and a model that includes vertical transport that drives the nitrogen and carbon chemistry out of equilibrium. The red curve (lower thin line) is the best fitting model in chemical equilibrium (model A from Table 2, with  $K_{zz} = 0$ ) and the blue curve (upper thin line) is the best fitting non-equilibrium model (model B with  $K_{zz} = 10^6 \text{ cm}^2 \text{ s}^{-1}$ ). The data and the noise spectrum are shown by the histograms (black). The uncertainty on the flux calibration of the IRS spectrum is  $\pm 5\%$ . The model fluxes, which have not been normalized to the data, are shown at the resolving power of the IRS spectrum ( $\lambda/\Delta\lambda = 90$ ). [See the electronic edition of the Journal for a color version of this figure.]

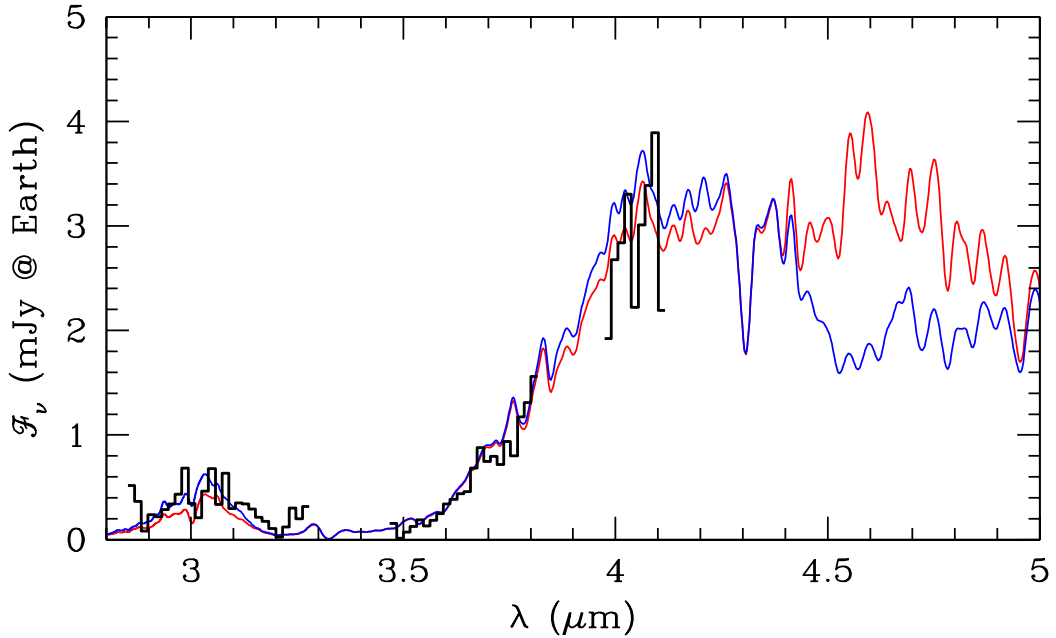


Fig. 6.— Comparison of the 2.9–4.1  $\mu\text{m}$  spectrum of 2MASS J0415–0935 with representative models in and out of chemical equilibrium. The red (dotted) curve is model B with  $K_{zz} = 0$  (chemical equilibrium) and the blue curve is model B with  $K_{zz} = 10^4 \text{ cm}^2 \text{ s}^{-1}$ . The appearance of the  $4.7 \mu\text{m}$  band of CO due to non-equilibrium chemistry can be seen in the models between 4.4 and  $4.9 \mu\text{m}$ . The data is shown by the black histogram. The model fluxes have not been normalized to the data and are shown at a resolving power of  $\lambda/\Delta\lambda = 200$ . [See the electronic edition of the Journal for a color version of this figure.]

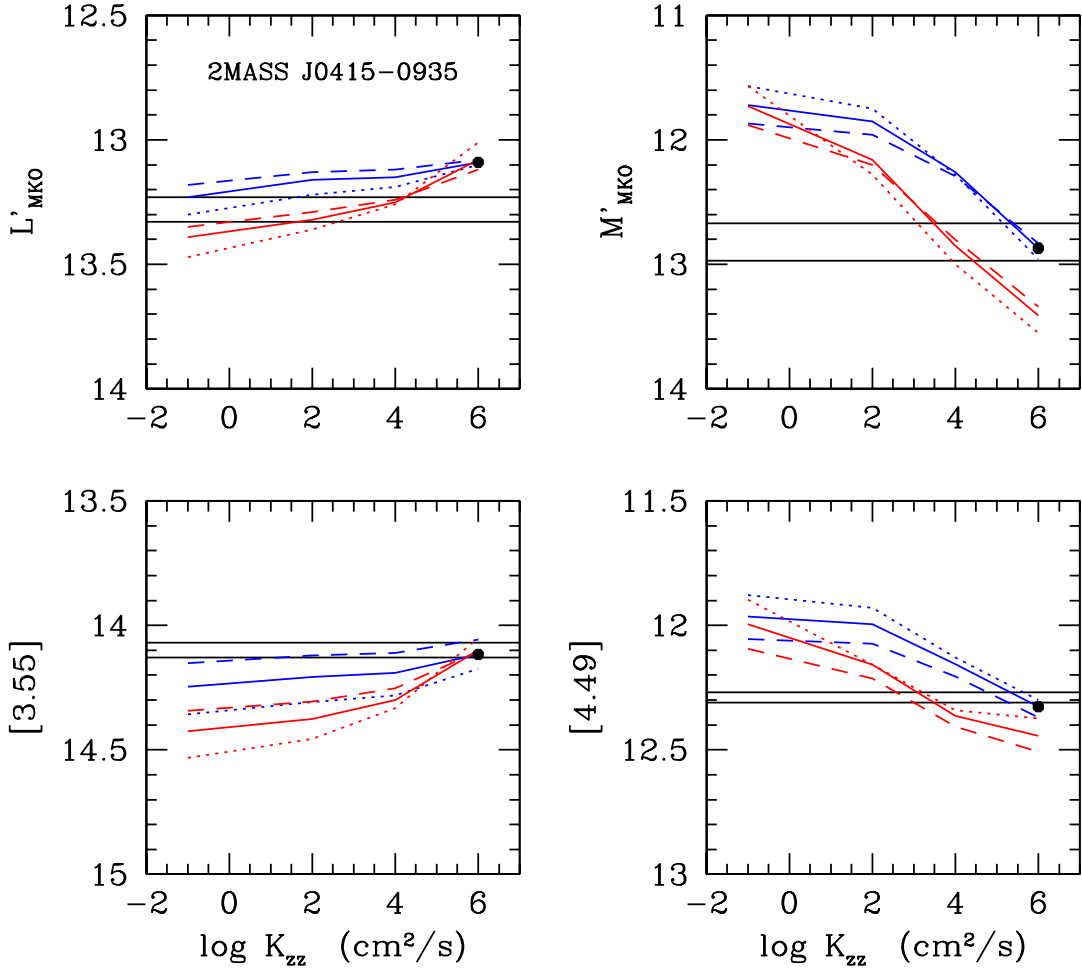


Fig. 7.— MKO and IRAC photometry of 2MASS J0415–0935 as a function of the coefficient of eddy diffusion for a range of models. Observed values ( $\pm 1\sigma$ ) are shown by the horizontal black lines. Synthetic photometry for each of the models in Table 2 is shown by the various curves: dotted lines: models A and A'; solid lines: models B and B'; dashed lines: models C and C'. Blue curves are for  $[\text{Fe}/\text{H}] = 0$  and red curves for  $[\text{Fe}/\text{H}] = +0.3$ , the latter are always below the former for a given pair of models. The solid dots show the values for a representative best fit model (see Figure 8). Models with  $K_{zz} = 0$  (in chemical equilibrium) are plotted at  $\log K_{zz} = -1$ . [See the electronic edition of the Journal for a color version of this figure.]

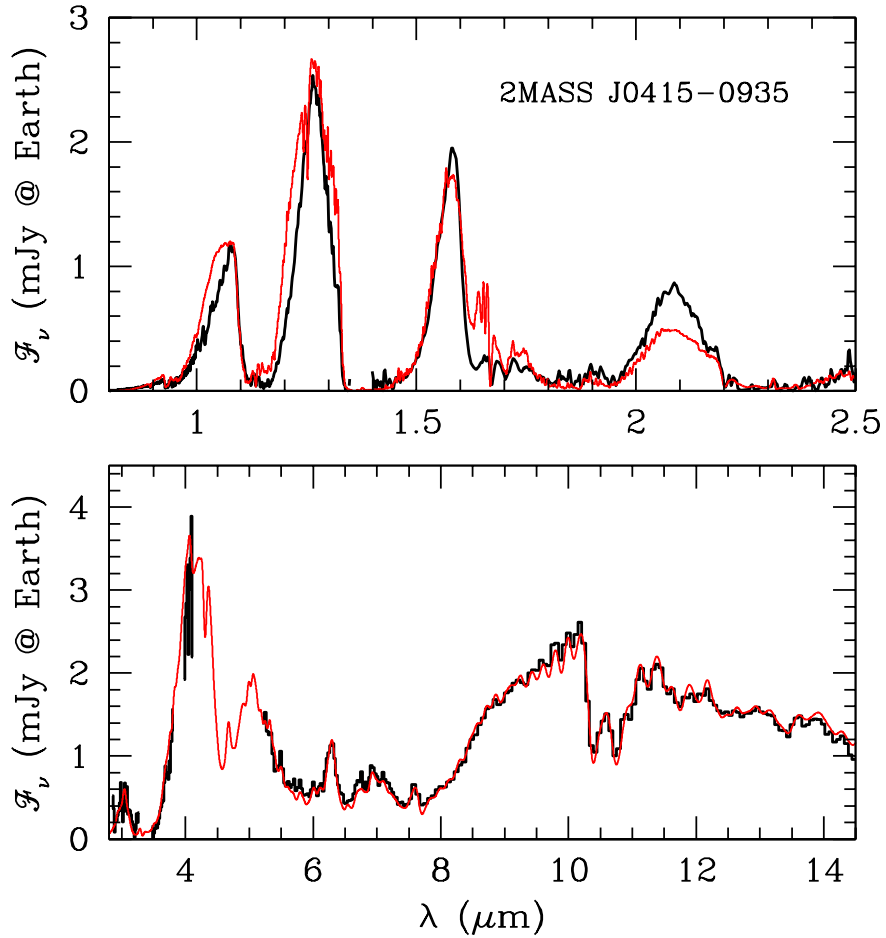


Fig. 8.— A model spectrum that represents a typical best fit of all the spectroscopic and photometric data for 2MASS J0415–0935. The model parameters are  $[\text{Fe}/\text{H}] = 0$ ,  $T_{\text{eff}} = 730$  K,  $\log g = 5.035$  (model B in Table 2) and an eddy diffusion coefficient of  $K_{zz} = 10^6 \text{ cm}^2 \text{ s}^{-1}$ . Model spectra are shown at a resolving power of  $\lambda/\Delta\lambda = 500$  (upper panel) and 90 (lower panel) to approximately match that of the data. The model fluxes have not been normalized to the data (heavy black line). [See the electronic edition of the Journal for a color version of this figure.]

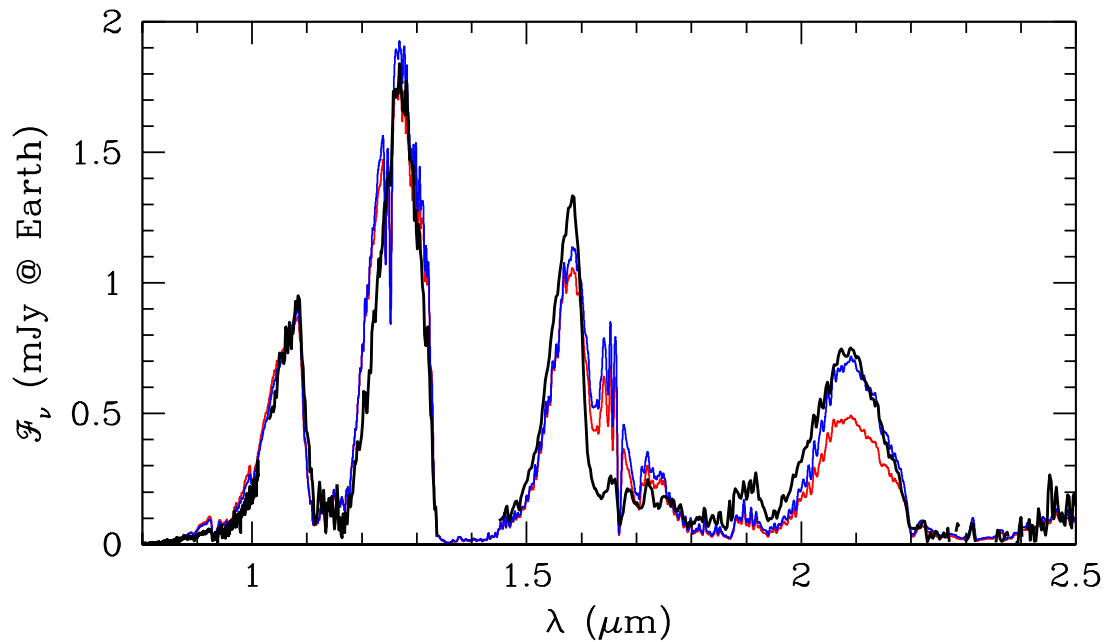


Fig. 9.— Comparison of the optical through near-infrared spectrum of 2MASS J1217–0311 with models of different metallicities. The red curve (lower thin line) is the best fitting model with  $[\text{Fe}/\text{H}]=0$  (model D) and the blue curve (upper thin line) is the best fitting model with  $[\text{Fe}/\text{H}]=+0.3$  (model E'). Both models assume chemical equilibrium ( $K_{zz} = 0$ ). The model fluxes have not been normalized to the data but have been smoothed to a resolving power of  $\lambda/\Delta\lambda = 500$  to approximate that of the data. The data is shown by the heavy black line. [See the electronic edition of the Journal for a color version of this figure.]

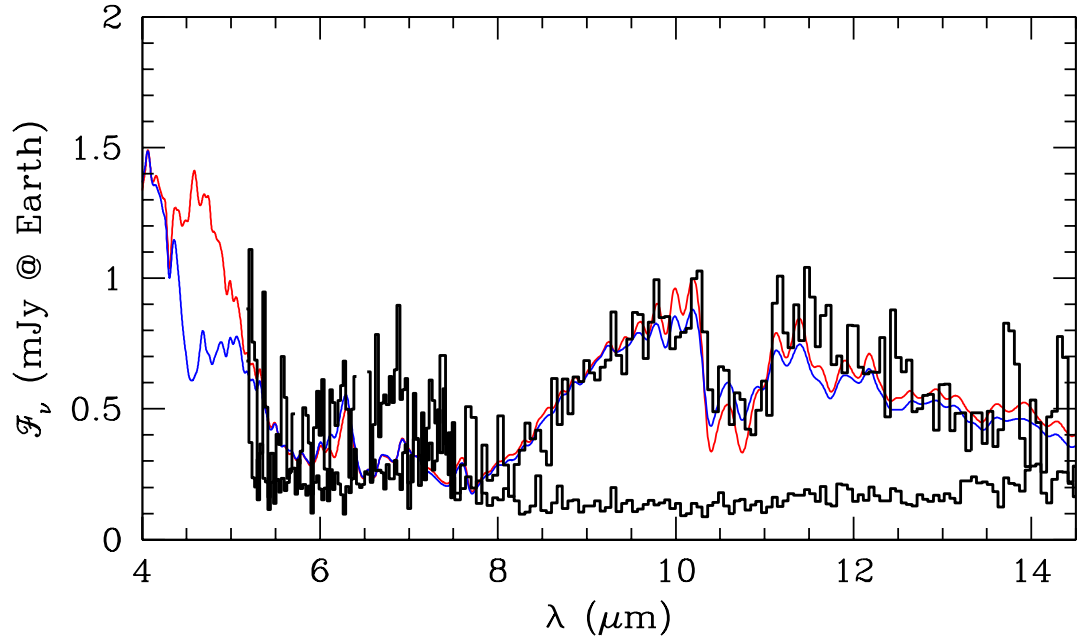


Fig. 10.— Fits of the IRS spectrum of 2MASS J1217–0311 showing the difference between a model in chemical equilibrium and a model that includes vertical transport that drives the nitrogen and carbon chemistry out of equilibrium. The red curve (upper thin line) is the best fitting model in chemical equilibrium (model E' from Table 3, with  $K_{zz} = 0$ ) and the blue curve (lower thin line) is a representative non-equilibrium model (model F' with  $K_{zz} = 10^2 \text{ cm}^2 \text{ s}^{-1}$ ). The data and the noise spectrum are shown by the histograms (black). The uncertainty on the flux calibration of the IRS spectrum is  $\pm 18\%$ . The model fluxes, which have not been normalized to the data, are shown at the resolving power of the IRS spectrum ( $\lambda/\Delta\lambda = 90$ ). [See the electronic edition of the Journal for a color version of this figure.]

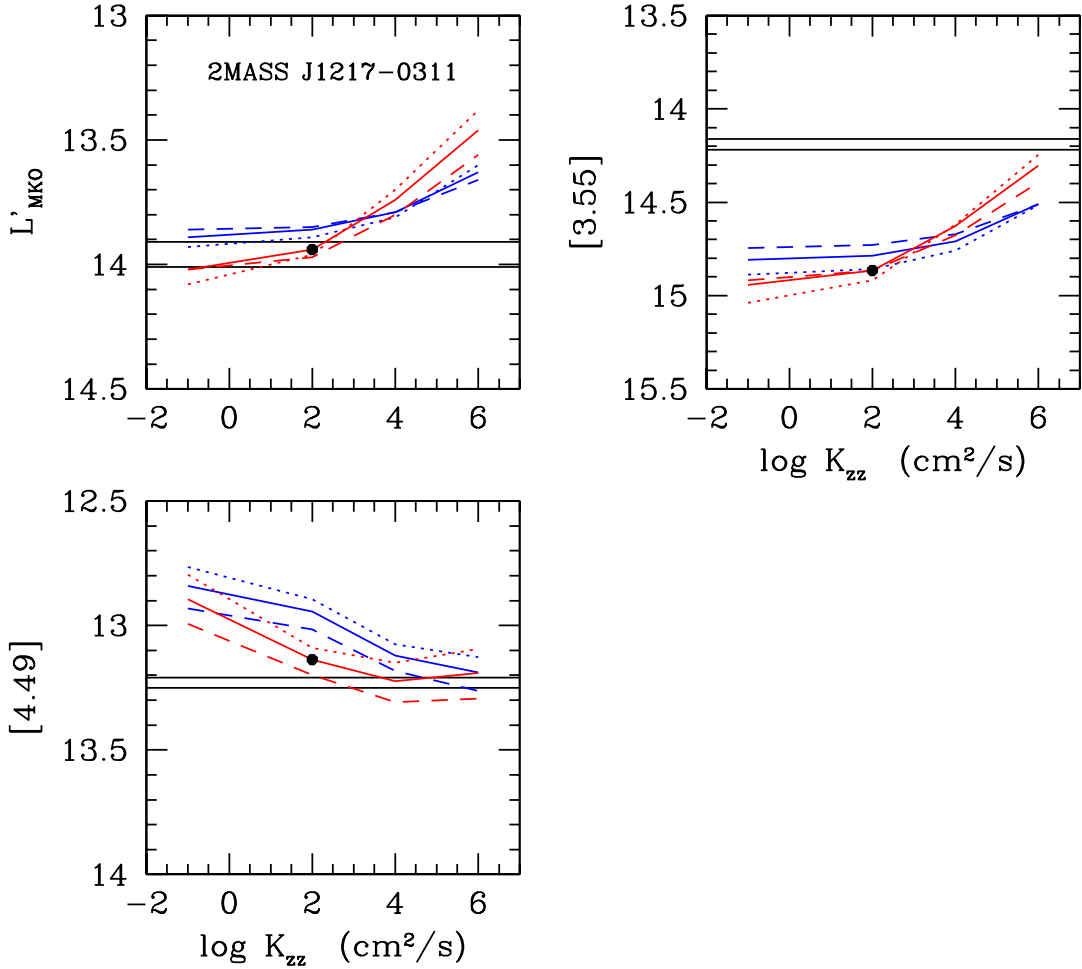


Fig. 11.— MKO and IRAC photometry of 2MASS J1217–0311 as a function of the coefficient of eddy diffusion for a range of models. Observed values ( $\pm 1\sigma$ ) are shown by the horizontal black lines. Synthetic photometry for each of the models in Table 3 is shown by the various curves: dotted lines: models D and D'; solid lines: models E and E'; dashed lines: models F and F'. Blue curves are for  $[\text{Fe}/\text{H}] = 0$  and red curves for  $[\text{Fe}/\text{H}] = +0.3$ , the latter are below the former for small  $K_{zz}$ . The solid dots show the values for a representative best fit model (see Figure 11). Models with  $K_{zz} = 0$  (in chemical equilibrium) are plotted at  $\log K_{zz} = -1$ . [See the electronic edition of the Journal for a color version of this figure.]

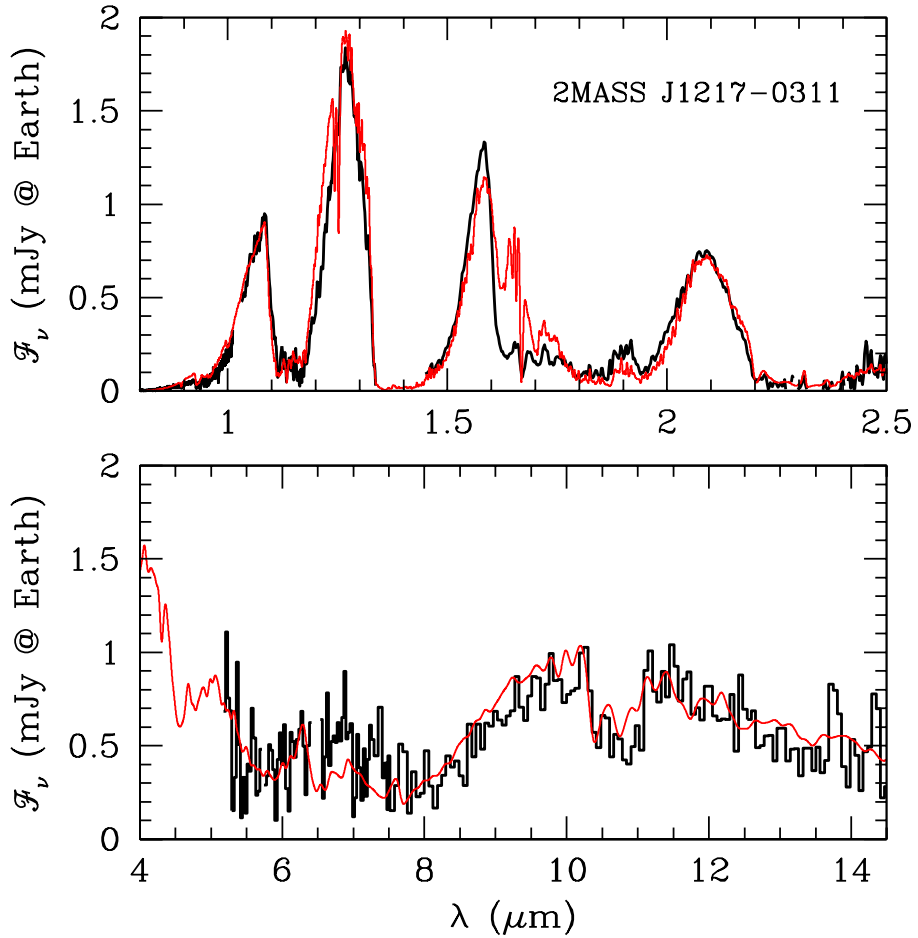


Fig. 12.— A model spectrum that represents a typical best fit of all the spectroscopic and photometric data for 2MASS J1217–0311. The model parameters are  $[\text{Fe}/\text{H}] = +0.3$ ,  $T_{\text{eff}} = 910\text{ K}$ ,  $\log g = 5.167$  (model E' in Table 3) and an eddy diffusion coefficient of  $K_{zz} = 10^2\text{ cm}^2\text{ s}^{-1}$ . Model spectra are shown at a resolving power of  $(\lambda/\Delta\lambda = 500$  (upper panel) and 90 (lower panel) to approximately match that of the data. The model fluxes have not been normalized to the data (heavy black curve). [See the electronic edition of the Journal for a color version of this figure.]